

# Full-wave analysis of extraordinary backscattering by a layered plasmonic nanosphere

You-Lin Geng,<sup>1</sup> Cheng-Wei Qiu,<sup>2,a)</sup> and Saïd Zouhdi<sup>3</sup>

<sup>1</sup>*Institute of Antenna and Microwaves, Hangzhou Dianzi University, Xiasha, Hangzhou, Zhejiang 310018, China*

<sup>2</sup>*Department of Electrical and Computer Engineering, National University of Singapore, Kent Ridge, Singapore 119260, Singapore*

<sup>3</sup>*Laboratoire de Génie Electrique de Paris, SUPELEC, Plateau de Moulon 91192, Gif-sur-Yvette, France*

(Received 30 October 2007; accepted 11 June 2008; published online 7 August 2008)

An exact full-wave analysis of plane-wave scattering by a multilayer nanosphere is proposed. The code is then used to study the behavior of N-layered plasmonic spherical particles. Our primary interest lies in achieving extraordinary scattering or transparency in the infrared regime by judicious pairing of plasmonic materials and control of the core-shell ratio. Numerical results and physical insights of these extraordinary phenomena are provided. © 2008 American Institute of Physics. [DOI: 10.1063/1.2966303]

## I. INTRODUCTION

Extraordinary scattering by nanoparticles has been receiving tremendous attention from research communities in both physics and engineering owing to its wide potential in data storage technology,<sup>1</sup> surface enhanced Raman scattering,<sup>2</sup> plasmonic antennas,<sup>3</sup> and plasmon resonance couplings.<sup>2,4</sup> According to the Rayleigh approximation, light scattering of a single nanosphere is dipolar.<sup>5,6</sup> Although the dipole paradigm for small particles has existed for centuries, the Rayleigh approximation was recently found to fail for a particular case of weakly dissipating materials near plasmon resonance frequencies,<sup>7</sup> where extraordinary scattering arises. We further extend the study to those unusual scatterings in spherically layered particles (the number of layers can be arbitrary) with the emphasis on the mechanism of interface plasmons (IPs) in the core-shell system. Such IPs are generated by particular combinations of the materials in the core-shell system and are localized at the interface. Note that they can be however coupled into the far-field scattering due to the radiative damping,<sup>8</sup> which gives rise to unusual properties in the far zone. If the radiative damping is not negligible anymore, the Rayleigh approximation is no longer valid. This motivates us to carry out a dynamic analysis for layered nanospheres with plasmonic materials.

In order to meet the requirement of IP generation, proper pairings of materials in the inner and outer layers are necessary. In view of this problem, we consider a special pairing, i.e.,  $\epsilon_1 \times \epsilon_2 < 0$  and  $\mu_1 \times \mu_2 < 0$ , where the subscripts denote the parameters in respective region. The idea of such special pairing was invoked by Alù and Engheta in the planar geometry<sup>9</sup> and later extended to the cylindrical tubes,<sup>10,11</sup> where giant optical resonance and resonance shifts were reported. In spherical geometries, nonmagnetic coated spheres were studied previously, such as the transparency of a single inclusion<sup>12</sup> and bulk resonance in the effective

permittivity.<sup>13–15</sup> The full-wave simulation, which can be found in many classical textbooks, was carried out in those works for either transparency or enhancement in two-layer spheres. However, it is still difficult to treat general materials with arbitrary constitutive parameters and sizes in each layer as well as arbitrary number of layers (i.e., more than two layers). It therefore gives us another motivation of this paper, aiming to extend the method in Ref. 5 to the study of arbitrarily multilayered plasmonic spheres especially in the infrared regime (IR). Also, rigorous predictions of extraordinary scattering properties will be investigated.

In the IR or visible regime, negative material parameters can be realized in certain noble metals and artificial metamaterials. The exotic electromagnetic properties in metamaterials have been well investigated for desired dielectric functions, ranging from negative to low positive values<sup>16–20</sup> by distributing resonant conducting rods in a matrix. To create the negative permeability, one can use the split-ring resonators.<sup>21,22</sup> Efforts have been made to investigate the potential optical applications of metamaterials, e.g., cloaking and transparency.<sup>23–25</sup> In the IR, negative permittivity and positive permeability are easy to realize by Drude materials, while it is difficult to achieve negative  $\epsilon$  and  $\mu$  simultaneously. Until recently, the polar crystalline has been explored to create double negative materials in IR.<sup>26,27</sup> Therefore, the materials studied in this paper are realizable in practice.

To obtain an exact solution to extraordinary scattering of a layered plasmonic nanosphere, an extension of the rigorous Mie theory is derived to model the scattering properties of multilayer plasmonic nanospheres (e.g., three-layer, four-layer, etc.). We start by expanding the electromagnetic fields by vector wave eigenfunctions (VWEFs). Thus, the electromagnetic fields in each layer are expressed via VWEFs weighted by their unknown scattering coefficients.<sup>28</sup> By applying the continuity of tangential components at each interface, these unknown coefficients are determined in an analytical algorithm where orthogonality relations of the Legendre polynomials are employed. After the present

<sup>a)</sup>Also at Laboratoire de Génie Electrique de Paris, SUPELEC. Electronic mail: eleqc@nus.edu.sg.

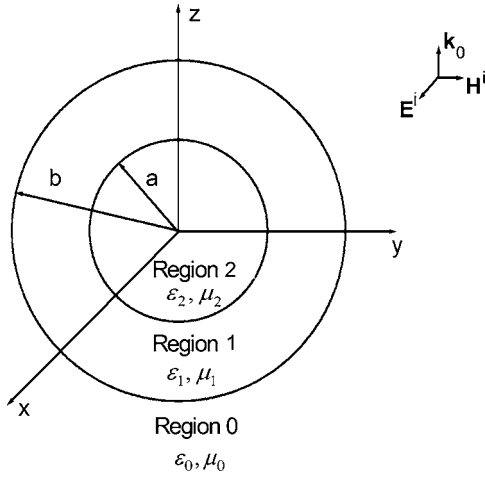


FIG. 1. Geometry for plane-wave scattering by the concentric isotropic sphere.

method is validated by comparing with these existing data, the relationship between the extraordinary scattering and IPs is fully explored.

## II. FORMULATION

The geometry of the cross-sectional view of a concentric sphere is shown in Fig. 1. The sphere can be divided into two homogeneous spherical layers whose outer and inner radii are  $b$  and  $a$ , respectively. Regions are denoted as regions 0–2. In our formulation and later numerical calculations, region 0 ( $r \geq b$ ) is assumed to be the free space. In the subsequent analysis, a time dependence of  $e^{-i\omega t}$  is assumed but suppressed throughout the treatment.

This composite structure is illuminated by a plane wave propagating in the  $+\hat{z}$ -direction with the electric field polarized along  $\hat{x}$ . The electromagnetic fields in region 2 can be expressed in terms of spherical VWEFs in isotropic medium as follows<sup>5,28–30</sup> ( $r \leq a$ , designated by the subscript 2):

$$\mathbf{E}_2 = \sum_{m,n} [A_{mn}^{(2)} \mathbf{M}_{mn}^{(1)}(\mathbf{r}, k_2) + B_{mn}^{(2)} \mathbf{N}_{mn}^{(1)}(\mathbf{r}, k_2)], \quad (1)$$

$$\mathbf{H}_2 = \frac{k_2}{i\omega\mu_{2m,n}} \sum_{m,n} [A_{mn}^{(2)} \mathbf{N}_{mn}^{(1)}(\mathbf{r}, k_2) + B_{mn}^{(2)} \mathbf{M}_{mn}^{(1)}(\mathbf{r}, k_2)]. \quad (2)$$

We can also obtain the electromagnetic fields in region 1 ( $a \leq r \leq b$ , designated by the subscript 1),

$$\mathbf{E}_1 = \sum_{l=1}^2 \sum_{m,n} [A_{mn}^{(l1)} \mathbf{M}_{mn}^{(l)}(\mathbf{r}, k_1) + B_{mn}^{(l1)} \mathbf{N}_{mn}^{(l)}(\mathbf{r}, k_1)], \quad (3)$$

$$\mathbf{H}_1 = \frac{k_1}{i\omega\mu_{1l}} \sum_{l=1}^2 \sum_{m,n} [A_{mn}^{(l1)} \mathbf{N}_{mn}^{(l)}(\mathbf{r}, k_1) + B_{mn}^{(l1)} \mathbf{M}_{mn}^{(l)}(\mathbf{r}, k_1)]. \quad (4)$$

The incident wave fields (designated by the superscript inc) may be expanded into an infinite series of spherical VWEFs as follows:<sup>29–34</sup>

$$\mathbf{E}^{\text{inc}} = \sum_{m,n} [\delta_{m,1} + \delta_{m,-1}] [a_{mn}^x \mathbf{M}_{mn}^{(1)}(\mathbf{r}, k_0) + b_{mn}^x \mathbf{N}_{mn}^{(1)}(\mathbf{r}, k_0)], \quad (5)$$

$$\mathbf{H}^{\text{inc}} = \frac{k_0}{i\omega\mu_{0mn}} \sum_{m,n} [\delta_{m,1} + \delta_{m,-1}] [a_{mn}^x \mathbf{N}_{mn}^{(1)}(\mathbf{r}, k_0) + b_{mn}^x \mathbf{M}_{mn}^{(1)}(\mathbf{r}, k_0)], \quad (6)$$

where

$$a_{mn}^x = \begin{cases} i^{n+1} \frac{2n+1}{2n(n+1)}, & m=1, \\ i^{n+1} \frac{2n+1}{2}, & m=-1, \end{cases} \quad (7)$$

$$b_{mn}^x = \begin{cases} i^{n+1} \frac{2n+1}{2n(n+1)}, & m=1, \\ -i^{n+1} \frac{2n+1}{2}, & m=-1, \end{cases} \quad (8)$$

$$\delta_{s,l} = \begin{cases} 1 & s=l \\ 0 & s \neq l \end{cases}. \quad (9)$$

According to the radiation condition of an outgoing wave and the asymptotic behavior of spherical Bessel functions, only  $h_n^{(1)}$  should be retained in the radial function, therefore the scattering fields (designated by the superscript  $s$ ) are expanded as

$$\mathbf{E}^s = \sum_{mn} [A_{mn}^s \mathbf{M}_{mn}^{(3)}(\mathbf{r}, k_0) + B_{mn}^s \mathbf{N}_{mn}^{(3)}(\mathbf{r}, k_0)], \quad (10)$$

$$\mathbf{H}^s = \frac{k_0}{i\omega\mu_{0mn}} \sum_{mn} [A_{mn}^s \mathbf{N}_{mn}^{(3)}(\mathbf{r}, k_0) + B_{mn}^s \mathbf{M}_{mn}^{(3)}(\mathbf{r}, k_0)], \quad (11)$$

where  $\mathbf{M}_{mn}^{(l)}(\mathbf{r}, k)$  and  $\mathbf{N}_{mn}^{(l)}(\mathbf{r}, k)$  are solenoidal spherical vector wave functions given

$$\mathbf{M}_{mn}^{(l)}(\mathbf{r}, k) = z_n^{(l)}(kr) \left[ im \frac{P_n^m(\cos \theta)}{\sin \theta} e^{im\phi} \hat{\theta} - \frac{dP_n^m(\cos \theta)}{d\theta} e^{im\phi} \hat{\phi} \right], \quad (12)$$

$$\mathbf{N}_{mn}^{(l)}(\mathbf{r}, k) = n(n+1) \frac{z_n^{(l)}(kr)}{kr} P_n^m(\cos \theta) e^{im\phi} \hat{r} + \frac{1}{kr} \frac{d(rz_n^{(l)}(kr))}{dr} \left[ \frac{dP_n^m(\cos \theta)}{d\theta} \hat{\theta} + im \frac{P_n^m(\cos \theta)}{\sin \theta} \hat{\phi} \right] e^{im\phi}, \quad (13)$$

where  $z_n^{(l)}$  represents an appropriate kind of spherical Bessel functions  $j_n$ ,  $y_n$ ,  $h_n^{(1)}$ , and  $h_n^{(2)}$ , for  $l=1, 2, 3$ , and  $4$ , respectively. The wavenumber can be expressed as  $k_i = \omega \sqrt{\epsilon_i} \sqrt{\mu_i}$  ( $i=0, 1, 2$ ).

After expanding the electromagnetic fields in spherical VWEFs, the unknown coefficients  $A_{mn}^{(2)}$  and  $B_{mn}^{(2)}$  in Eqs. (1) and (2) in region 2,  $A_{mn}^{(l1)}$  and  $B_{mn}^{(l1)}$  ( $l=1$  and  $2$ ) in Eqs. (3) and (4) in region 1, and the scattering coefficients  $A_{mn}^s$  and

$B_{mn}^s$  can be determined by the tangential-component continuity of electromagnetic fields at each interface. The boundary conditions at  $r=a$  and  $r=b$  are written as

$$E_{2,t} = E_{1,t}, \quad (14)$$

$$H_{2,t} = H_{1,t}, \quad (15)$$

$$E_{1,t} = E_t^{\text{inc}} + E_{0,t}^s, \quad (16)$$

$$H_{1,t} = H_t^{\text{inc}} + H_{0,t}^s. \quad (17)$$

Substituting Eqs. (1)–(6), (10), and (11) into Eqs. (14)–(17), the following expressions of expansion coefficients can be obtained:

$$\begin{aligned} & \begin{bmatrix} j_n(k_1 a) y_n(k_1 a) & y_n(k_1 a) \\ \frac{k_1}{\mu_1} R_n^{(1)}(k_1 a) & \frac{k_1}{\mu_1} R_n^{(2)}(k_1 a) \end{bmatrix} \begin{bmatrix} A_{mn}^{(11)} \\ A_{mn}^{(21)} \end{bmatrix} \\ &= \begin{bmatrix} j_n(k_2 a) \\ \frac{k_2}{\mu_2} R_n^{(1)}(k_2 a) \end{bmatrix} A_{mn}^{(2)}, \end{aligned} \quad (18)$$

$$\begin{aligned} & \begin{bmatrix} j_n(k_1 b) & y_n(k_1 b) \\ \frac{k_1}{\mu_1} R_n^{(1)}(k_1 b) & \frac{k_1}{\mu_1} R_n^{(2)}(k_1 b) \end{bmatrix} \begin{bmatrix} A_{mn}^{(11)} \\ A_{mn}^{(21)} \end{bmatrix} \\ &= \begin{bmatrix} h_n^{(1)}(k_0 b) \\ \frac{k_0}{\mu_0} R_n^{(3)}(k_0 b) \end{bmatrix} A_{mn}^s + \begin{bmatrix} j_n(k_0 b) \\ \frac{k_0}{\mu_0} R_n^{(1)}(k_0 b) \end{bmatrix} \\ & \quad \times a_{nm}^x [\delta_{m,-1} + \delta_{m,1}], \end{aligned} \quad (19)$$

$$\begin{bmatrix} R_n^{(1)}(k_1 a) & R_n^{(2)}(k_1 a) \\ \frac{k_1}{\mu_1} j_n(k_1 a) & \frac{k_1}{\mu_1} y_n(k_1 a) \end{bmatrix} \begin{bmatrix} B_{mn}^{(11)} \\ B_{mn}^{(21)} \end{bmatrix} = \begin{bmatrix} R_n^{(1)}(k_2 a) \\ \frac{k_2}{\mu_2} j_n(k_2 a) \end{bmatrix} B_{mn}^{(2)}, \quad (20)$$

$$\begin{aligned} & \begin{bmatrix} R_n^{(1)}(k_1 b) & R_n^{(2)}(k_1 b) \\ \frac{k_1}{\mu_1} j_n(k_1 b) & \frac{k_1}{\mu_1} y_n(k_1 b) \end{bmatrix} \begin{bmatrix} B_{mn}^{(11)} \\ B_{mn}^{(21)} \end{bmatrix} \\ &= \begin{bmatrix} R_n^{(3)}(k_0 b) \\ \frac{k_0}{\mu_0} h_n^{(1)}(k_0 b) \end{bmatrix} B_{mn}^s + \begin{bmatrix} R_n^{(3)}(k_0 b) \\ \frac{k_0}{\mu_0} j_n(k_0 b) \end{bmatrix} \\ & \quad \times b_{nm}^x [\delta_{m,-1} + \delta_{m,1}], \end{aligned} \quad (21)$$

where  $R_n^{(l)}(kr) = (1/kr) d[rz_n^{(l)}(kr)]/dr$  and  $z_n^{(l)}$  denotes the spherical Bessel function of the  $l$ th kind with the order  $n$  as motioned before. The scattering coefficients  $A_{mn}^s$  and  $B_{mn}^s$  can be obtained by solving Eqs. (18)–(21). If the layer number is bigger (e.g., 3 or 4), the coefficient chain can be straightforwardly extended, and all coefficients involved in the matrices can be solved systematically. Then the scattering cross section (SCS) of the concentric sphere by a plane wave can be calculated, and the back-SCS is expressed as

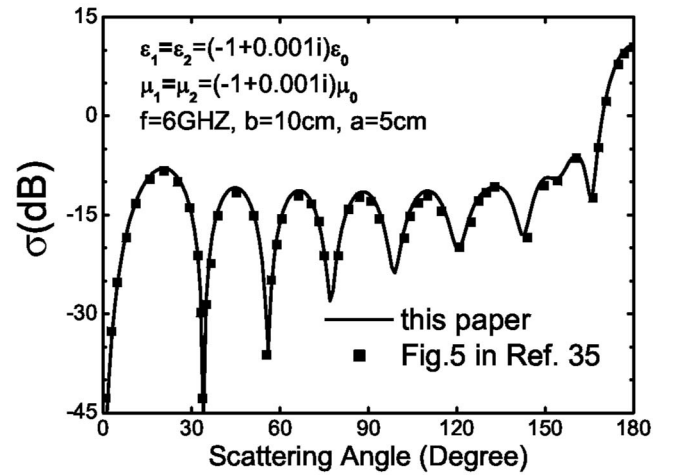


FIG. 2. Radar cross sections (RCSs) vs scattering angle  $\theta$  (in degrees). Comparison of RCSs between a homogeneous double negative sphere in Ref. 35 and the concentric negative sphere where the mediums in regions 1 and 2 are set to be identical. The frequency of the incident wave is 6 GHz, the radii are chosen as  $b=10$  cm and  $a=5$  cm, and medium parameters are assumed to be  $\epsilon_1/\epsilon_0 = \epsilon_2/\epsilon_0 = \mu_1/\mu_0 = \mu_2/\mu_0 = -1 + 0.001i$ . The sign of the imaginary parts is opposite to that in Ref. 35 due to the selection of time dependence.

$$\begin{aligned} \sigma|_{\theta=\pi, \phi=0} &= \lim_{r \rightarrow \infty} 4\pi r^2 \left. \frac{|E^s|^2}{|E^i|^2} \right|_{\theta=\pi, \phi=0} \\ &= \frac{\pi}{k_0^2} \left[ \sum_{n=1}^{\infty} i^n \{ [n(n+1)B_{1n}^s - B_{-1n}^s] \right. \\ & \quad \left. - [n(n+1)A_{1n}^s + A_{-1n}^s] \right]^2 \\ & \quad + \left[ \sum_{n=1}^{\infty} i^{n+1} \{ [n(n+1)B_{1n}^s + B_{-1n}^s] \right. \\ & \quad \left. - [n(n+1)A_{1n}^s - A_{-1n}^s] \right]^2. \end{aligned} \quad (22)$$

### III. VALIDATION AND DISCUSSION

In Sec. II, we have presented the theoretical formulation for the scattering of an electromagnetic plane wave by a concentric sphere. To gain more physical insights into this problem, we will provide and discuss particular numerical examples in this section.

In order to check the correctness of our method, we compare our results to the work of Monzon *et al.*<sup>35</sup> based on Bor-Carlos calculations. Since there are no reported full-wave results of scattering by concentric plasmonic spheres, we calculate the concentric model where the parameters in the core and shell are equally negative so as to have the same setting as in Ref. 35. Very good agreement can be seen in Fig. 2, where the truncation of  $n$  used in Eqs. (18)–(21) is chosen to be 22. Thus, it partially verifies the correctness and applicability of our present full-wave analysis as well as the program codes. In what follows, we will study some specific cases which lead to interesting phenomena.

Figure 3 shows the dependence of SCSs in terms of the ratio  $a/b$  for a dielectric particle ( $\epsilon_2 = 4\epsilon_0$ ) covered by an

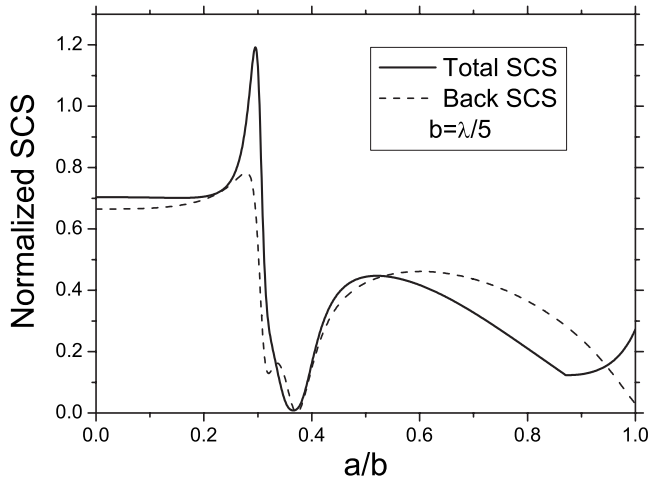
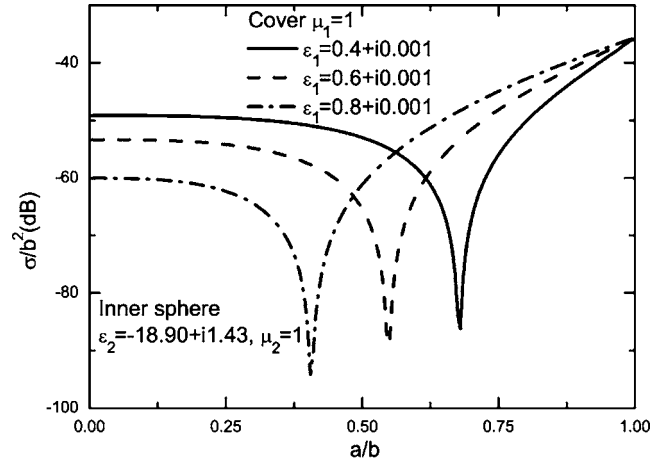


FIG. 3. SCS normalized by the factor of  $\lambda^2$  vs ratio of radius of inner core to the cover ( $a/b$ ), where permittivity and permeability in the core are  $\epsilon_2 = 4\epsilon_0$  and  $\mu_2 = \mu_0$ , and those in the cover are  $\epsilon_1 = -3\epsilon_0$  and  $\mu_1 = \mu_0$ .

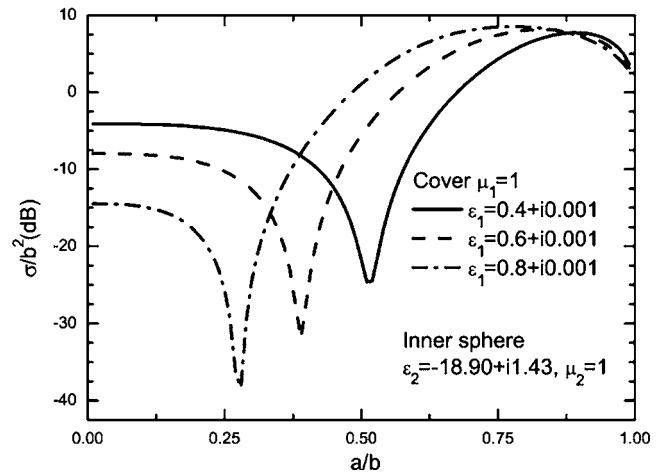
$\epsilon$ -negative (ENG) layer with ( $\epsilon_1 = -3\epsilon_0$ ).<sup>9,10</sup> The outer radius  $b = 0.2\lambda$ , where  $\lambda$  is the wavelength of the incident wave. Of particular interest is the comparison between Fig. 3 in our paper and the last picture of Fig. 3 in Ref. 12. Why do the two figures depicting the same case give different results? The problem may stem from the theoretical preliminaries (it can be easily verified by computing the total SCS in the limiting case of  $a/b = 0$ , i.e., a homogeneous sphere with radii  $b$ ,  $\epsilon_1$ , and  $\mu_1$ ). Further simulation reveals that our results agree well with those in Ref. 12 for the case of small particles. When the particle size is comparable to the incidence wavelength (e.g.,  $0.2\lambda$ ), quasistatic approximation would lose its accuracy. Instead, the full-wave analysis in this paper has no restriction. It is also worth noting that it seems physically more suitable to say “scattering reduction” rather than “invisibility” when  $a/b = 0.01$  since the SCS values with or without the plasmonic cover are always very close to zero over the whole range of  $a/b$ . Besides, Fig. 3 reveals that for  $b = 0.2\lambda$ , the presence of the plasmonic cover increases the SCS of the uncoated case (i.e.,  $a/b = 1$ ) except for a small region in the vicinity of the critical ratio at  $a/b \approx 0.37$ .

Next, let us consider the scattering properties of coated nanoparticles involving noble metals at infrared frequencies. Figure 4 reports the back-SCSs of a gold sphere coated by a dielectric whose relative permittivity is less than unity. In Fig. 4(a), it is shown that the SCS value for uncoated Au nanoparticles at 441 THz is about  $-36$  dB when its radius is  $0.01\lambda$ , and if the sphere is completely occupied by the dielectrics of  $\epsilon_1 = 0.8 + 0.001i$ , for instance, the normalized SCS is about  $-60$  dB. Initiatively, SCS values of the Au nanoparticles coated by such dielectrics may be in between these limiting values, as expected. However, the back-SCS experiences a drastic reduction within a range of  $a/b$  in the vicinity of critical ratio of  $a/b = 0.406$ , which can be attributed to the coupling of near-zone surface polaritons to far-field quantities owing to the radiative damping.

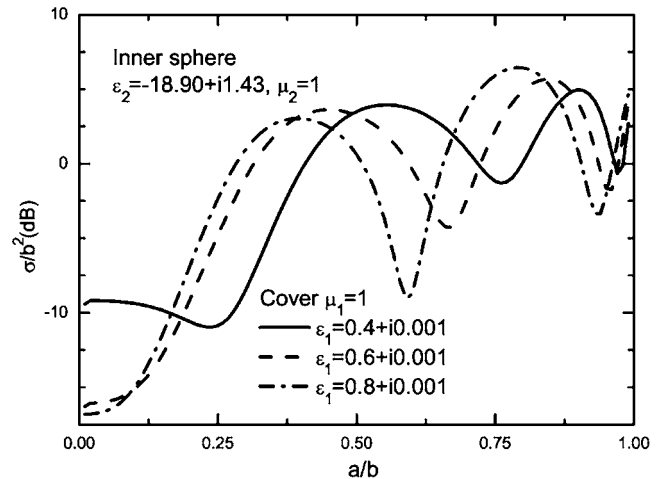
Each curve in Fig. 4(a) possesses its critical ratio (i.e.,  $0.68$  for the line of  $\epsilon_1 = 0.4 + 0.001i$ ;  $0.55$  for  $\epsilon_1 = 0.6$



(a)  $b = 0.01\lambda$ ,  $\lambda$  is the wavelength of incident wave



(b)  $b = 0.25\lambda$ ,  $\lambda$  is the wavelength of incident wave



(c)  $b = 0.5\lambda$ ,  $\lambda$  is the wavelength of incident wave

FIG. 4. Normalized back-SCS vs radii ratio for Au nanoparticles coated by different dielectrics at 441 THz, and different physical sizes of the coated sphere are considered: (a) electrically small ( $b = 0.01\lambda$ ), (b) medium ( $b = 0.25\lambda$ ), and (c) comparable to wavelength ( $b = 0.5\lambda$ ). The optical parameters of gold are obtained from Ref. 36.

+  $0.001i$ ; and  $0.406$  for  $\epsilon_1 = 0.8 + 0.001i$ ), which shifts toward the lower end if the permittivity of the cover is approaching to unity. It seems that the critical ratio is primarily affected by the permittivity of the cover. Since the size of the particles is only  $\lambda/100$ , the quasistatic approximation for zero

reflection [see Eq. (5.36) in Ref. 5 p. 149] is still valid. Hence, from polarizability theory, these critical ratios are found to be  $\text{Re}[\sqrt[3]{((\epsilon_1 - \epsilon_0)(2\epsilon_1 + \epsilon_2) / (2\epsilon_1 + \epsilon_0)(\epsilon_1 - \epsilon_2))}]$ . The critical ratio in Fig. 4(b) where reflection reduction occurs also agrees with that calculated by the theoretical formula. However, the aforementioned formula cannot be used when the particle size is comparable to the wavelength. As shown in Fig. 4(c), it seems that the volume oscillation, which is negligible in the cases of Figs. 4(a) or 4(b), comes into play, leading to the failure of the theoretical prediction of critical ratios.

Figure 5 shows that if the cover is a low-permittivity dielectric, the backscattering patterns versus core-shell ratio are analogous in near infrared frequencies. The critical ratios for scattering reduction are only dependent on the permittivity of the cover. It is also found that when the size of the particle is comparable to the wavelength, the contribution due to the volume oscillation becomes obvious regardless of the illumination.

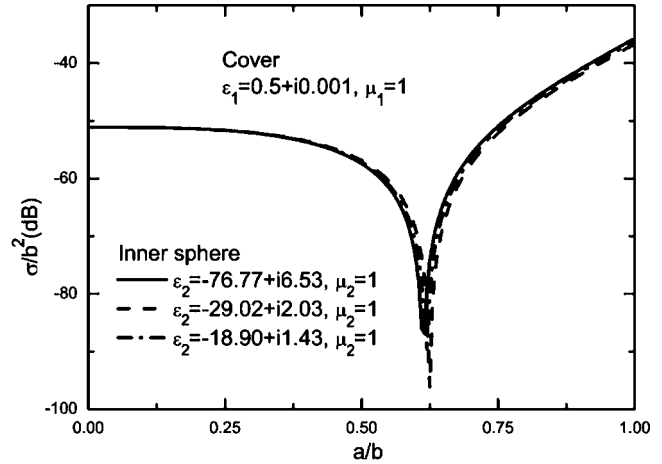
Previously, nanosized gold particles covered with a lossless dielectric whose permittivity is less than unity are considered. In Fig. 6, a high-permittivity polymer  $\text{Al}_2\text{O}_3$  is used as the cover of the gold sphere. Interestingly, critical ratios corresponding to zero backscattering never arise, and backscattering patterns differ at various near infrared frequencies. In the cases of 242 and 360 THz with a fixed outer radius of  $0.01\lambda$ , the back-SCS increases with the volume of the inner metal sphere. However, when the frequency keeps increasing (e.g., 441 THz), there appear ranges of ratios where SCS decreases with the volume of the inner metal sphere. It is of particular interest to note that both scattering suppression and enhancement occur to the cases shown in Figs. 6(b) and 6(c). The oscillation against the core-shell ratio becomes more drastic and complicated, which is in contrast to the situation of the low-permittivity cover in Fig. 5. Thus, the fine control of the radii plays a more significant role in the extraordinary scattering diagrams for high-permittivity coating of gold nanoparticles.

Note that the electric-type and magnetic-type polarizabilities of such concentric sphere can be obtained by making some reduction from the results of<sup>37</sup>

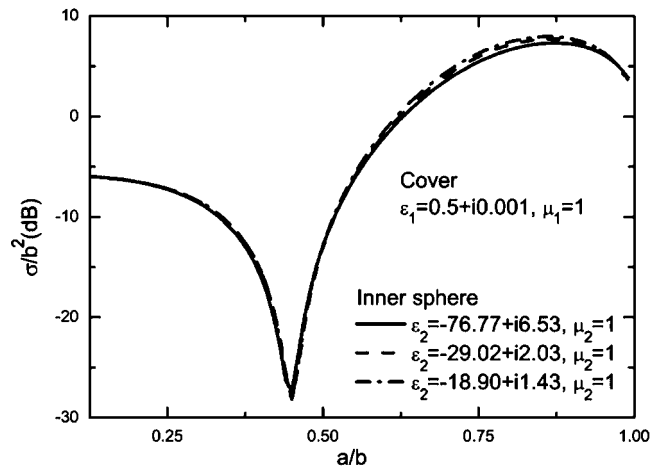
$$\alpha_e = \frac{4\pi b^3 \epsilon_0}{\Delta} \{ [(\mu_1 + 2)(\epsilon_1 - 1) + (\mu_1 - 1)(2\epsilon_1 + 1)(a/b)^3] \times [(\mu_2 + 2\mu_1)(\epsilon_2 + 2\epsilon_1) + 2(\mu_2 - \mu_1)(\epsilon_2 - \epsilon_1) \times (a/b)^3] - 9(a/b)^3 [2\epsilon_1^2 \mu_1^2 + \epsilon_1 \mu_1 (\mu_2 - 2\epsilon_2) - \epsilon_2 \mu_2] \}, \quad (23)$$

$$\alpha_m = \frac{4\pi b^3 \epsilon_0}{\Delta} \{ [(\mu_1 - 1)(\epsilon_1 + 2) + (2\mu_1 + 1)(\epsilon_1 - 1)(a/b)^3] \times [(\mu_2 + 2\mu_1)(\epsilon_2 + \epsilon_1) + 2(\mu_2 - \mu_1)(\epsilon_2 - \epsilon_1)(a/b)^3] - 9(a/b)^3 [2\epsilon_1^2 \mu_1^2 + \epsilon_1 \mu_1 (\epsilon_2 - 2\mu_2) - \epsilon_2 \mu_2] \}, \quad (24)$$

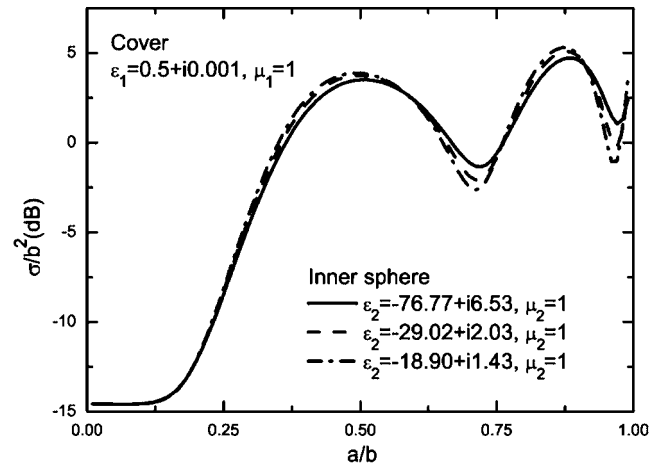
where



(a)  $b=0.01\lambda$ ,  $\lambda$  is the wavelength of incident wave



(b)  $b=0.25\lambda$ ,  $\lambda$  is the wavelength of incident wave



(c)  $b=0.5\lambda$ ,  $\lambda$  is the wavelength of incident wave

FIG. 5. Normalized back-SCS vs radii ratio for Au nanospheres coated by a low-permittivity cover and illuminated at 242 THz (solid line), 360 THz (dashed line), and 441 THz (dot-dashed line), respectively. Those gold nanospheres are coated by the same low-permittivity cover of  $\epsilon_1 = 0.5 + i0.001i$ . (a) electrically small ( $b=0.01\lambda$ ), (b) medium ( $b=0.25\lambda$ ), and (c) comparable to wavelength ( $b=0.5\lambda$ ).

$$\Delta = [(\mu_1 + 2)(\epsilon_1 + 2) + 2(\mu_1 - 1)(\epsilon_1 - 1)(a/b)^3] [(\mu_2 + 2\mu_1)(\epsilon_2 + 2\epsilon_1) + 2(\mu_2 - \mu_1)(\epsilon_2 - \epsilon_1)(a/b)^3] - 18(a/b)^3 (\epsilon_1 \mu_1 - \epsilon_2)(\epsilon_1 \mu_1 - \mu_2). \quad (25)$$

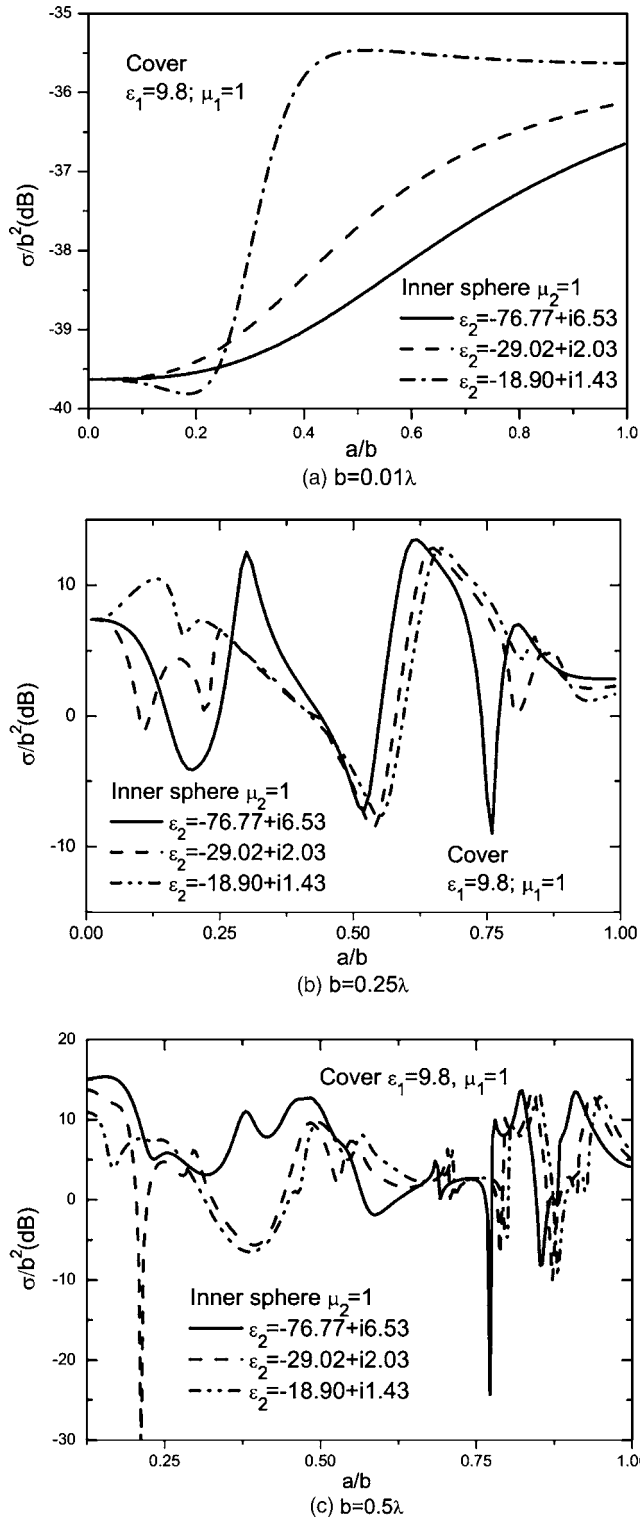


FIG. 6. Normalized backscattering vs ratio of the radii for Au nanospheres coated by high-permittivity polymer  $\text{Al}_2\text{O}_3$  at 242 THz (solid line), 360 THz (dashed line), and 441 THz (dot-dashed line).

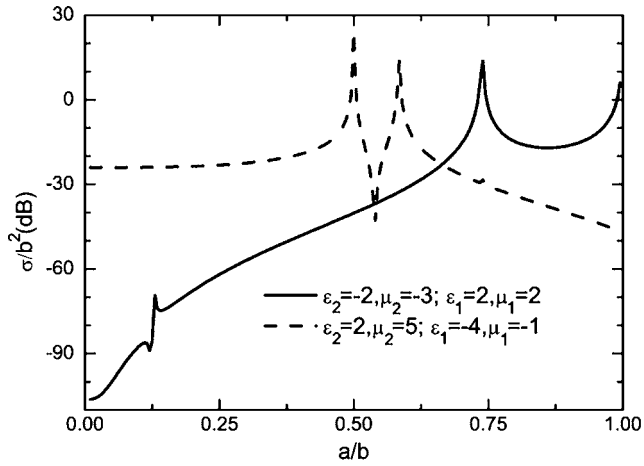
Hence, it is clear that the *transparency* requires the numerators in Eqs. (23) and (24) to be zero, from where the critical ratio of  $a/b$  can be yielded by the formula presented before. It can be also explained with the induced dipole moments in the core and shell. The transparency actually implies the radiation due to the dipole moment in the core is canceled by that due to the dipole induced in the shell. If the parameters

are lossy, the solved  $a/b$  is also a complex number, where only the real parts within (0, 1) make sense. It can be verified that for conventional dielectric covers as in Figs. 4 and 5, the critical ratios of  $a/b$  only exist when  $\epsilon_1 < 1$ . In a more detailed range, one can further differentiate the three critical ratios in Fig. 5(a) by zero-polarizability conditions, which are 0.626 for the solid line, 0.619 for the dashed line, and 0.613 for the dot-dashed line. In the other circumstances, e.g., Fig. 6, the real parts of  $a/b$  will be either higher than 1 or negative, which are not physical. It can also be attributed to the fact that  $\epsilon_1 < 0$  or  $\epsilon_1 > 1$  would result in a negative magnetic polarizability and makes the effective permeabilities ( $\mu_{\text{eff}}$ ) far from that of free space, which leads to high observability no matter how the core-shell ratio is adjusted.

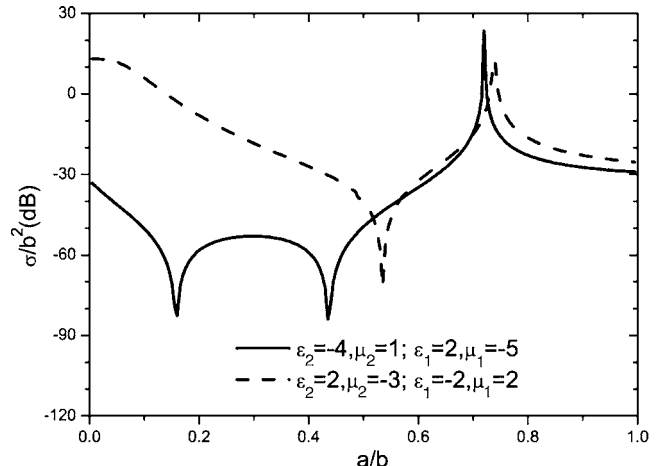
The phenomena of transparency and scattering enhancement become more complicated in the case of conjugate combinations:  $\epsilon_1 \times \epsilon_2 < 0$  and  $\mu_1 \times \mu_2 < 0$ . Such conjugate pairings in planar<sup>38</sup> and cylindrical geometries<sup>10</sup> have presented some peculiar properties such as scattering enhancement, transparency, and wave tunneling. For the conjugate pairings, we mainly consider two combinations of materials of the inner core and the cover: (1) double positive (DPS)-double negative (DNG) and (2) ENG- $\mu$ -negative (MNG). Our full-wave simulations of conjugate pairings in spherical geometry give a more complete picture than the pioneering work by Alù and Engheta. Although we can study conjugate pairing for an arbitrary number of layers, the two-layered case is our emphasis in this paper.

The backscatterings of DPS-DNG and ENG-MNG pairings are reported in Figs. 7 and 8, respectively. Since the polarizabilities are dependent on both permittivities and permeabilities, the exact transparency therefore needs a critical ratio where both  $a_e$  and  $a_m$  vanish. This is impossible to predict by using quasistatic approximation in most of the cases. However, the hybrid effects can be analyzed by our dynamic method. The interface between two conjugate spherical layers supports interface resonance. The ratio  $a/b$  plays an important part in affecting the backscattering properties. Judicious selection of conjugate composites in the core-shell system and the ratio of  $a/b$  could provide us possibilities to control the scattering properties, either suppression or amplification. For instance, in the combination of a conventional core and left-handed cover as the dot line in Fig. 7(a), the backscattering varies drastically along the ratio from 0.5 to 0.6, experiencing two enhancement peaks and one suppression peak. The variations of scattering diagrams for slightly bigger nanospheres, as shown in Figs. 7(b) and 7(c), are more complicated when the core-shell ratio is controlled.

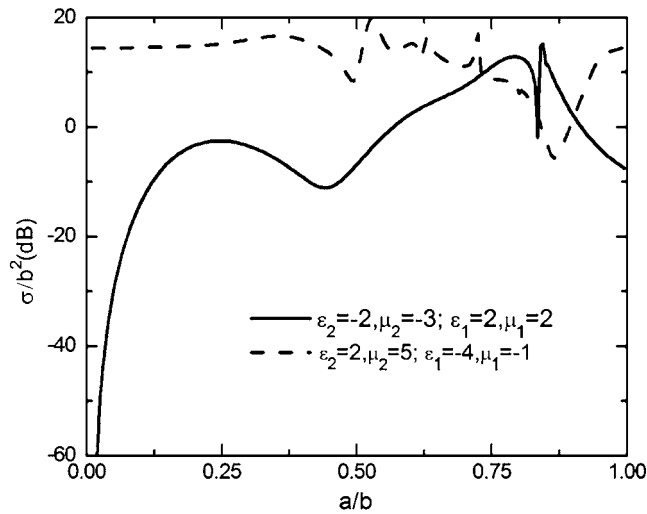
On the other hand, in the ENG (core) and MNG (cover) combination in nanoscale (see Fig. 8), a sensitive *ratio bandwidth* ranges from 0.4 to 0.8 in Fig. 8(a), where the backscattering magnitude increases drastically from  $-86$  to  $+25$  dB. Hence, such coated nanoparticle sized at  $0.01\lambda$  becomes quite detectable by the external medical instruments as if it was a dielectric object with a large cross section. For bigger sizes of ENG-MNG pairings, there are also many interesting observations of the radii ratio. For example, in the solid line of Fig. 8(b), (i.e., ENG in the core and MNG in the



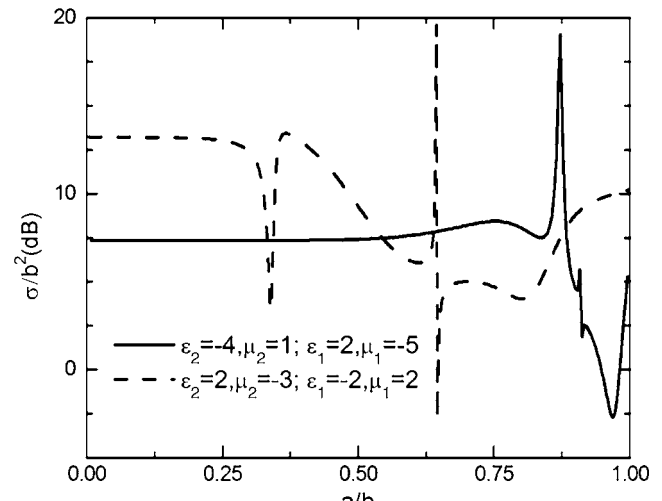
(a)  $b=0.01\lambda$



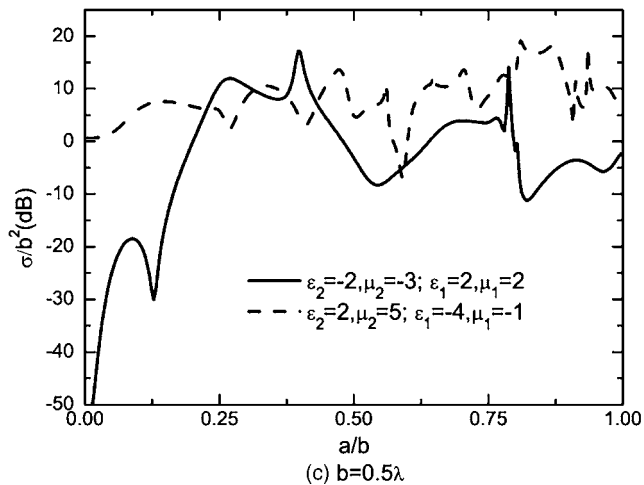
(a)  $b=0.01\lambda$



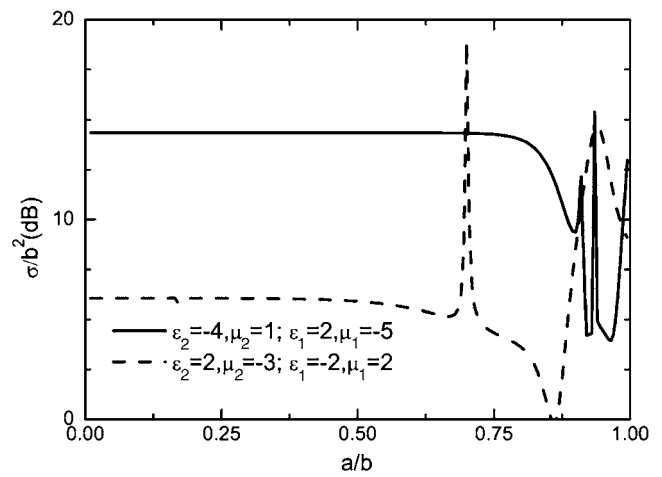
(b)  $b=0.25\lambda$



(b)  $b=0.25\lambda$



(c)  $b=0.5\lambda$



(c)  $b=0.5\lambda$

FIG. 7. Backscattering of DPS-DNG combinations for core-shell pairings in nanoscale.

FIG. 8. Backscattering of ENG-MNG combinations for core-shell pairings in nanoscale.

cover), the backscattering is not very sensitive to the core-shell ratio until it is near  $a/b \approx 0.87$ , where a drop of 23 dB in SCS occurs. Also, similar insensitive ratio bandwidths are observed for both ENG-MNG and MNG-ENG pairings in Fig. 8(c) when  $a/b$  is not big, but the amplification in SCS when  $a/b \approx 0.7$  in the dashed line of Fig. 8(c) is quite inter-

esting. This result could be of great interest in applications such as data storage, Raman scattering based applications, and medical diagnosis since very small objects can exhibit remarkably enhanced backscattering, making them easier to be observed.

Next, let us consider a dispersive cover characterized by the Drude model. The permeability of a Drude medium is  $\mu_0$ , and the permittivity carries the following form:

$$\epsilon_D = \epsilon_0 \left\{ 1 - \frac{1}{\left(\frac{\omega}{\omega_p}\right)^2 + \left(\frac{\Gamma}{\omega_p}\right)^2} + i \frac{\left(\frac{\Gamma}{\omega_p}\right)}{\left(\frac{\omega}{\omega_p}\right) \left[ \left(\frac{\omega}{\omega_p}\right)^2 + \left(\frac{\Gamma}{\omega_p}\right)^2 \right]} \right\}, \quad (26)$$

where  $\omega$  is the incidence frequency,  $\omega_p$  is the plasma frequency, and  $\Gamma/\omega_p$  is the dissipation factor. There are two particular considerations for back-SCS: (1) the role of core-shell ratio with the working frequency near  $\omega_p$  and (2) the role of working frequency with fixed core-shell ratio.

When  $\omega \approx \omega_p$ , the permittivity of a Drude model with weak dissipation can be approximated as

$$\frac{\epsilon_D}{\epsilon_0} \approx i \frac{\Gamma}{\omega_p}. \quad (27)$$

$\text{Al}_2\text{O}_3$  ceramic is considered as the inner core in Fig. 9, coated by a Drude material operating in the vicinity of  $\omega_p$ . If the size is extremely small, e.g., Fig. 9(a), it is found that the SCS has negligible variation with the ratio ( $a/b$ ) from 0 to 0.75, meaning the increase in the size of the inner dielectric core hardly contributes below a *threshold* value of  $a/b$ . Analogous threshold ratios can be observed in larger sizes in Figs. 9(b) and 9(c), which shift downward due to the volume resonances. In other words, backscattering is more sensitive to the ratio in the presence of a thin (e.g.,  $0.8 < a/b < 1$ ) coating of Drude materials at  $\omega_p$ . Drastic oscillations can be observed in the thin Drude coating, for instance, a fine change in the core-shell ratio near  $a/b \approx 0.84$  may result in a variation of 40 dB in the backscattering cross section. When the Drude coating is thin, the role of the damping is also remarkable even if the dampings in all cases are very weak.

Figure 10 presents the backscattering versus frequency for different nanosizes. There are two limiting cases: (1) when  $\omega$  is much smaller than  $\omega_p$ , the real part of the permittivity of a Drude material is negative and (2) if  $\omega$  is higher than  $\omega_p$ , the real part of the permittivity is approaching that of free space. Therefore, the enhancement will occur when  $\omega/\omega_p$  is small, as shown in Fig. 10. In Fig. 10(b), highly oscillated profiles occur to both cases for  $a/b=0.5$  and  $a/b=0.75$  in the region  $0.05 < \omega/\omega_p < 0.12$ , where the coated system becomes quite detectable even if its size is very small (still in the range of infrared frequencies). The reduction in the backscattering can also be observed at properly chosen frequencies.

In addition to the interesting results presented above, there are several advantages of the exact solution proposed here, compared to previous works. First, our method is capable of studying the scattering at any specified angle for layered structures, while Ref. 7 studied some particular cases only based on the well established identities,<sup>5</sup> which are valid for a single sphere only.<sup>29,31</sup> Second, our work can be easily tailored to the study of multilayered plasmonic spheres by utilizing similar ideas to determine multiple scatterings as in Ref. 34, which established the dyadic Green's functions for multilayered anisotropic spheres to consider dipole illumination.

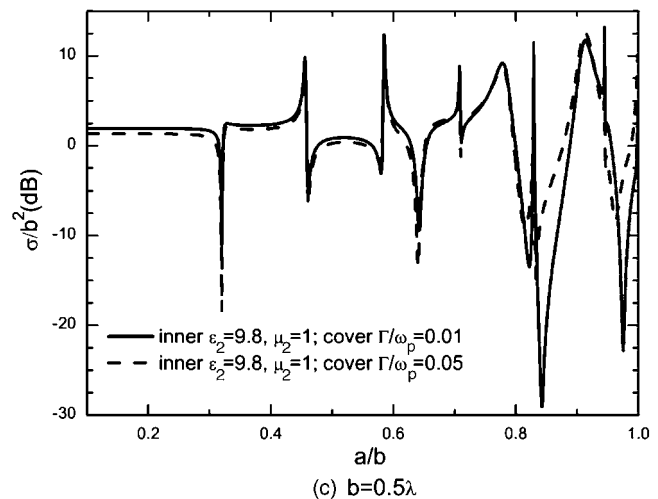
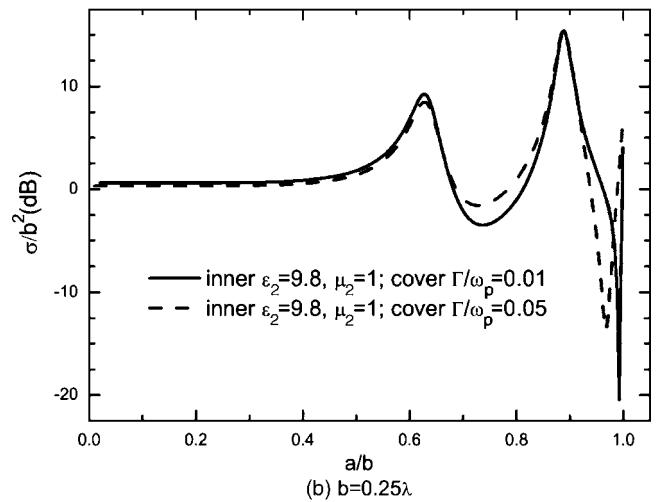
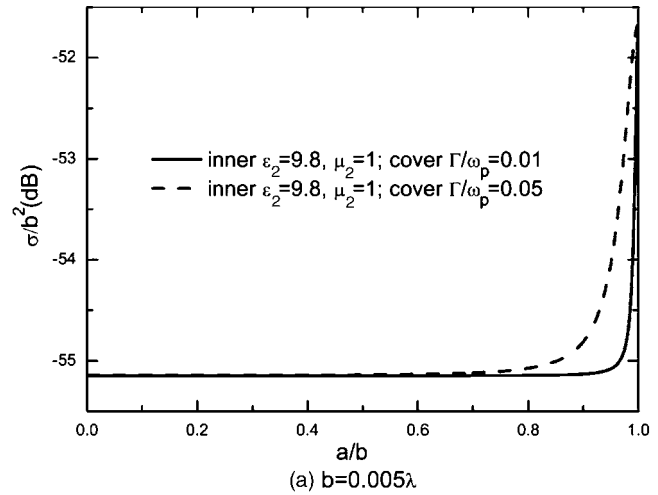


FIG. 9. Back-SCS vs  $a/b$  at different nanosizes, when the cover is a Drude material working at the plasma frequency.

For instance, the backscattering of a multilayered nanosphere is considered in Fig. 11(a) where the innermost and outermost layers are filled by ceramics and the intermediate shell is occupied by a Drude material. In Fig. 11(b), we consider the backscattering dependence upon frequency of a homogeneous Drude sphere, and the outer radius  $c$  is kept unchanged [the same as in Fig. 11(a),  $c=0.05\lambda$ ]. Therefore,

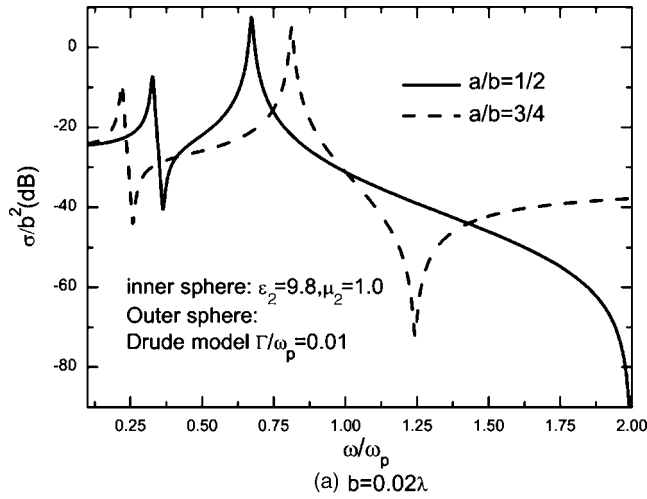
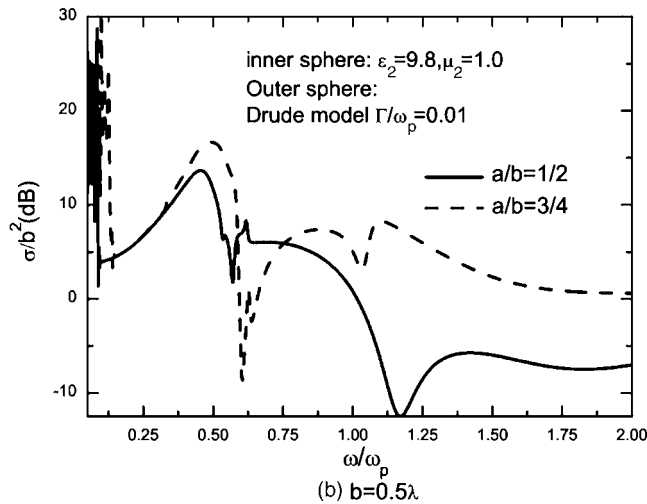
(a)  $b=0.02\lambda$ (b)  $b=0.5\lambda$ 

FIG. 10. Backscattering vs incidence frequency for a two-layer particle at different nanosizes. The inner core is filled with  $\text{Al}_2\text{O}_3$  ceramic and the cover is a Drude material. The frequency has been normalized by the plasma frequency  $\omega_p$ . In (a), the outer radius  $b$  is fixed at  $0.02\lambda$ , and  $b=0.5\lambda$  for (b). In each case, two core-shell ratios are considered, and the resonances are presented.

Figs. 11(a) and 11(b) have the same physical size, and thus the role of the sandwich structure in Fig. 11(a) can be demonstrated clearly. It is observed that there exist two resonant frequencies in Fig. 11(a) due to the interface polaritons while only one resonance occurs in the case of a homogeneous Drude sphere in Fig. 11(b). Moreover, the multiple resonances in backscattering are more sensitive than the single resonance in Fig. 11(b) to the incident frequency. It implies that the interface polariton in the multilayer nanosphere could be manipulated to modulate sensitive resonances in backscattering, which is useful in medical engineering. For instance, in the vicinity of those two resonant frequencies, the variation in the backscattering is quite drastic with respect to the incident frequency, and such observation sensitivity can be easily recorded on external devices, giving a possibility of detecting certain abnormal bodies in biomedical applications.

#### IV. CONCLUSION

In this paper, the full-wave analysis using VWEFs in an inhomogeneous medium has been carried out to characterize

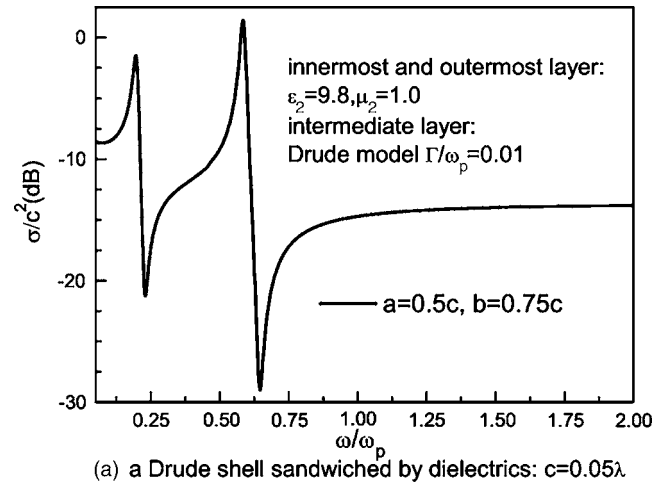
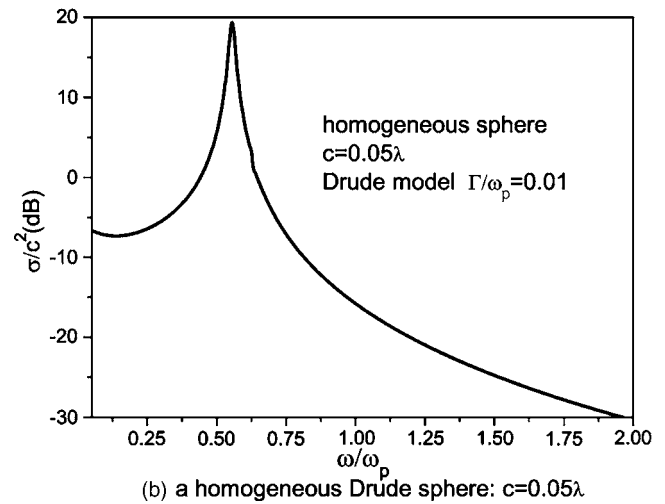
(a) a Drude shell sandwiched by dielectrics:  $c=0.05\lambda$ (b) a homogeneous Drude sphere:  $c=0.05\lambda$ 

FIG. 11. Backscattering of a three-layer nanoparticle with a Drude material sandwiched by  $\text{Al}_2\text{O}_3$  ceramic, compared to the backscattering of a homogeneous Drude particle at the same outer radius  $c$ .  $c$  denotes the radius of the outermost spherical surface, while  $a$  and  $b$  still represent the two radii of inner shells.

the extraordinary scattering of plasmonic core-shell systems and plasmonic multilayered spheres. Owing to the robustness and capability of the derived full-wave method, the three-dimensional scattering of a plane wave by a layered plasmonic sphere has been extensively studied and commented. We provide an analytical and general method to investigate the role of local IPs in achieving extraordinary scattering diagrams, especially in layered structures. Numerical examples and physical interpretations are presented to emphasize how the core-shell ratio should be designed for desired scattering patterns (e.g., constructive or destructive diagrams). Potential applications in cloaking and amplification of targets' SCS were presented. The role of IPs excited at the junctions of adjacent layers needs to be investigated further in future.

#### ACKNOWLEDGMENTS

The authors are grateful to the financial supports from SUMMA Foundation, U.S.A. We also acknowledge Grant No. Y104539 of the Natural Science Foundation of Zhejiang Province (China).

- <sup>1</sup>Z. B. Wang, B. S. Luk'yanchuk, M. H. Hong, Y. Lin, and T. C. Chong, *Phys. Rev. B* **70**, 035418 (2004).
- <sup>2</sup>J. P. Kottmann and O. J. F. Martin, *Opt. Express* **8**, 655 (2001).
- <sup>3</sup>P. Mühlischlegel, H. J. Eisler, O. J. F. Martin, B. Hecht, and D. W. Pohl, *Science* **308**, 1607 (2005).
- <sup>4</sup>K. Li, M. I. Stockman, and D. J. Bergman, *Phys. Rev. Lett.* **91**, 227402 (2003).
- <sup>5</sup>C. F. Bohren and D. R. Huffman, *Absorption and Scattering of Light by Small Particles* (Wiley, New York, 1998).
- <sup>6</sup>M. Born and E. Wolf, *Principles of Optics*, 7th ed. (Cambridge University Press, Cambridge, 1999).
- <sup>7</sup>M. I. Tribelsky and B. S. Luk'yanchuk, *Phys. Rev. Lett.* **97**, 263902 (2006).
- <sup>8</sup>R. Fuchs and K. L. Kliewer, *J. Opt. Soc. Am.* **58**, 319 (1968).
- <sup>9</sup>A. Alù and N. Engheta, *IEEE Trans. Antennas Propag.* **51**, 2558 (2003).
- <sup>10</sup>C. W. Qiu, H. Y. Yao, S. N. Burokur, S. Zouhdi, and L. W. Li, *IEICE Trans. Commun.* **E90-B**, 2423 (2007).
- <sup>11</sup>H. Y. Yao, L. W. Li, C. W. Qiu, Q. Wu, and Z. N. Chen, *Radio Sci.* **42**, RS2006 (2007).
- <sup>12</sup>A. Alù and N. Engheta, *Phys. Rev. E* **72**, 016623 (2005).
- <sup>13</sup>A. Alù and N. Engheta, *J. Appl. Phys.* **97**, 094310 (2005).
- <sup>14</sup>A. Alù and N. Engheta, *J. Appl. Phys.* **99**, 069901 (2006).
- <sup>15</sup>X. M. Zhou and G. K. Hu, *Phys. Rev. E* **74**, 026607 (2006).
- <sup>16</sup>W. Rotman, *IEEE Trans. Antennas Propag.* **10**, 82 (1962).
- <sup>17</sup>S. O'Brien and J. B. Pendry, *J. Phys.: Condens. Matter* **14**, 4035 (2002).
- <sup>18</sup>J. B. Pendry, A. J. Holden, D. J. Robbins, and W. J. Stewart, *J. Phys.: Condens. Matter* **10**, 4785 (1998).
- <sup>19</sup>A. Alù, M. G. Silveirinha, A. Salandrino, and N. Engheta, *Phys. Rev. B* **75**, 155410 (2007).
- <sup>20</sup>A. N. Lagarkov, S. M. Matytsin, K. N. Rozanov, and A. K. Sarychev, *J. Appl. Phys.* **84**, 3806 (1998).
- <sup>21</sup>J. B. Pendry, A. J. Holden, D. J. Robbins, and W. J. Stewart, *IEEE Trans. Microwave Theory Tech.* **47**, 2075 (1999).
- <sup>22</sup>R. A. Shelby, D. R. Smith, and S. Schultz, *Science* **292**, 77 (2001).
- <sup>23</sup>A. Porch, D. V. Morgan, and R. M. Perks, *J. Appl. Phys.* **95**, 4734 (2007).
- <sup>24</sup>A. Alù and N. Engheta, *Opt. Express* **15**, 3318 (2007).
- <sup>25</sup>C. W. Qiu, S. Zouhdi, and Y. L. Geng, *Phys. Rev. E* **77**, 046604 (2008).
- <sup>26</sup>V. Yannopoulos and A. Moroz, *J. Phys.: Condens. Matter* **17**, 3717 (2005).
- <sup>27</sup>C. W. Qiu and L. Gao, *J. Opt. Soc. Am. B* (accepted).
- <sup>28</sup>D. Sarkar and N. J. Halas, *Phys. Rev. E* **56**, 1102 (1997).
- <sup>29</sup>H. C. Van de Hulst, *Light Scattering by Small Particles* (Dover, New York, 1981).
- <sup>30</sup>W. C. Chew, *Waves and Fields in Inhomogeneous Media* (Van Nostrand, New York, 1990).
- <sup>31</sup>O. B. Toon and T. P. Ackerman, *Appl. Opt.* **20**, 3657 (1981).
- <sup>32</sup>V. V. Varadan, A. Lakhtakia, and V. K. Varadan, *IEEE Trans. Antennas Propag.* **37**, 800 (1989).
- <sup>33</sup>C. W. Qiu, L. W. Li, T. S. Yeo, and S. Zouhdi, *Phys. Rev. E* **75**, 026609 (2007).
- <sup>34</sup>C. W. Qiu, S. Zouhdi, and A. Razek, *IEEE Trans. Antennas Propag.* **55**, 3515 (2007).
- <sup>35</sup>C. Monzon, D. W. Forester, and L. N. Medgyesi-Mitschang, *J. Opt. Soc. Am. A* **21**, 2311 (2004).
- <sup>36</sup>*Handbook of Optical Constants of Solids II*, edited by E. D. Palik (Academic, New York, 1991).
- <sup>37</sup>I. V. Lindell, A. H. Sihvola, S. A. Tretyakov, and A. J. Viitanen, *Electromagnetic Waves in Chiral and Bi-Isotropic Media* (Artech House, Boston, 1994).
- <sup>38</sup>M. G. Silveirinha, A. Alù, and N. Engheta, *Phys. Rev. E* **75**, 036603 (2007).